RSC Advances

PAPER

View Article Online
View Journal | View Issue

Cite this: *RSC Adv.*, 2026, **16**, 28558

Engineering nitrogen-doped carbon quantum dots: investigating the role of dopant isomer configuration

Maryam Rasouli,[a] Amir Rezvani-Moghaddam,[ab] Yuxin Liu,[a] Roxana Moaref,[a] Jinfeng Zhang [a] and Uttandaraman Sundararaj †*[a]

Nitrogen-doped carbon quantum dots (N-CQDs) have emerged as versatile nanomaterials whose optical and interfacial properties are highly sensitive to dopant chemistry. However, the role of dopant regiochemistry in governing nitrogen incorporation pathways and subsequent structure–property relationships is not well understood. In this work, N-CQDs were synthesized *via* a one-step microwave-assisted bottom-up approach using citric acid as the carbon source and *ortho*-, *meta*, and *para*-phenylenediamine (*o*-PD, *m*-PD, and *p*-PD) as nitrogen dopants to systematically investigate the influence of dopant configuration. Electron microscopy revealed that *o*- and *m*-PD promote the formation of spherical quantum dots with average sizes of 7.63 ± 1.65 and 9.44 ± 2.31 nm, respectively, whereas *p*-PD favors the growth of micrometer-scale carbon sheets. X-ray photoelectron spectroscopy demonstrates that dopant configuration strongly affects nitrogen bonding states, with *o*-PD yielding predominantly graphitic nitrogen, *m*-PD and *p*-PD incorporating nitrogen mainly as amide. These structural differences lead to pronounced variations in optical behavior: *o*-PD-derived N-CQDs exhibit excitation-independent blue photoluminescence with a quantum yield of 24%, while *m*-PD – derived N-CQDs show reduced emission efficiency (16%), and *p*-PD – derived products are largely non-emissive. To assess the solid-state functionality of the synthesized N-CQDs, they were incorporated into poly(vinyl alcohol) (PVA) matrices. The results reveal that dopant-dependent morphology and surface chemistry significantly influence the crystallization behavior, mechanical performance, and UV-shielding efficiency of the resulting nanocomposites. In particular, N-CQDs derived from *o*-PD enable effective UV blocking while maintaining high transparency in the visible region and enhancing the mechanical properties of the PVA matrix. The PVA nanocomposite film containing *o*-PD – derived CQDs demonstrates the ability to block around 90% of the UV radiation at 400 nm. Moreover, incorporation of *o*-PD – derived CQDs modestly increases the elastic modulus (2286 MPa) and tensile strength (50.3 MPa) compared with pure PVA (1965 MPa and 37.6 MPa, respectively), while substantially enhancing the elongation at break (26.3% *versus* 19.6%). Overall, this study elucidates how dopant regiochemistry governs early-stage nucleation, nitrogen incorporation, and interfacial interactions, providing insights to rationally design functional CQD-based nanocomposites.

Received 16th March 2026
Accepted 15th May 2026

DOI: 10.1039/d6ra02179d

rsc.li/rsc-advances

1 Introduction

Carbon quantum dots (CQDs) were first discovered as byproducts during single-walled carbon nanotube synthesis. CQDs are a novel class of carbon nanomaterials (approximately less than 10 nm in size) with distinctive optical and electronic properties. Their strong photoluminescence, efficient charge transfer, high water solubility, low toxicity, and biocompatibility make them promising for applications in bioimaging, sensing, photovoltaics, optoelectronics and UV-shielding applications.[1–4] Unlike traditional UV-shielding nanoparticles, CQDs provide strong UV absorption, excellent dispersibility in polymer matrices, and minimal impact on optical clarity and mechanical strength, while also being photostable and biocompatible. These features make CQDs a particularly promising alternative for next-generation UV-shielding polymer materials.[5]

Structurally, CQDs consist of a carbon-rich core comprising a mixture of amorphous and nanocrystalline domains, primarily composed of sp^2-hybridized carbon atoms forming a graphitic framework, surrounded by oxygen-containing surface functional groups that enhance their dispersibility in

[a]*Department of Chemical and Petroleum Engineering, University of Calgary, 2500 University Drive NW, Calgary, AB T2N 1N4, Canada. E-mail: ut@ucalgary.ca*

[b]*Faculty of Polymer Engineering, Sahand University of Technology, P.O. Box, 51335–1996, Tabriz, Iran*

† Deceased author: Professor Uttandaraman Sundararaj passed away on March 24, 2026.

aqueous media.[1,6,7] Similar to graphene, CQDs are carbon-based materials characterized by delocalized π electrons arising from the overlap of unhybridized p orbitals in sp^2 domains, which enable strong ultraviolet (UV) light absorption in both materials. However, CQDs are capable of re-emitting light. Unlike pristine graphene, which exhibits a zero bandgap due to the convergence of the valence and conduction bands at the dirac point, CQDs display semiconductor-like behavior with a finite, size-tunable bandgap. In graphene, the absence of a bandgap allows photoexcited electron–hole pairs to relax non-radiatively through continuum band states, thereby suppressing photoluminescence. Conversely, in CQDs, due to the size effects, pronounced quantum confinement and surface state effects discretize the electronic energy levels, leading to radiative recombination and efficient photoluminescence emission.[8–10] This confinement becomes significant as the particle size approaches the exciton Bohr radius, resulting in quantized energy levels and an increased bandgap relative to bulk carbon materials. Consequently, smaller CQDs require higher excitation energies and emit photons of shorter wavelengths upon relaxation, thus enabling precise modulation of the emission color through control of size and surface chemistry.[11,12]

Beyond size effects, heteroatom doping represents another effective strategy to tailor the electronic and optical properties of CQDs. The incorporation of dopant atoms introduces additional energy states within the bandgap or change the intrinsic bandgap, which can directly influence the absorption and emission characteristics of CQDs.[13] Since the atomic radius of nitrogen is comparable to that of carbon, and nitrogen atoms can be readily incorporated into the carbon framework, N-doped CQDs represent the most extensively studied and promising doping system.[14]

Several theoretical and experimental studies have demonstrated that nitrogen incorporation can significantly modify the electronic structure of CQDs by introducing additional electronic states and altering the density of states near the band edges. In particular, nitrogen doping can lead to an apparent bandgap narrowing through enhanced π-electron delocalization, along with the introduction of localized defect and surface states, both of which enable absorption of lower-energy photons and contribute to redshifted optical behavior. In UV-vis spectra, these effects are often manifested as additional absorption features attributed to $n \rightarrow \pi^*$ transitions, arising from the excitation of electrons from nonbonding orbitals associated with heteroatoms (*e.g.*, nitrogen or oxygen) to antibonding π* states. While nitrogen incorporation into the conjugated carbon framework can influence the intrinsic electronic structure of CQDs, the observed $n \rightarrow \pi^*$ transitions primarily reflect the presence of surface functional groups and defect-related electronic states within the carbon framework.[14] Consequently, nitrogen doping broadens the optical absorption profile of CQDs by both modulating the electronic band structure and introducing additional sub-bandgap states, thereby facilitating absorption at longer UV wavelengths. This enhanced and broadened UV absorption is particularly beneficial for UV-blocking applications.[15,16]

Extensive research has been conducted on tailoring the optical properties of CQDs through the use of various nitrogen-doping agents. Rosales *et al.*[17] employed four different nitrogen sources with distinct chemical characteristics, namely, diethanolamine, diethylamine, ethylenediamine, and 1,2-phenylenediamine, to investigate how the chemical and optical properties of the resulting N-doped CQDs are influenced by the structural features of the precursors. Their findings indicated that the positioning of amine groups at molecular terminals, as well as the presence of cyclic geometries, facilitated the incorporation of nitrogen into the CQD framework. In another study conducted by Nguyen *et al.*, citric acid was employed as the carbon source, while various nitrogen-containing dopants (urea, trizma base, beta-alanine, L-arginine and EDTA) were investigated to examine how the optical and band structure properties of the resulting N-doped carbon quantum dots (N-CQDs) were influenced by the precursors' reactivity, solubility, and molecular structure during the carbonization process.[18] However, there is a lack of comprehensive research on the effects of configuration of a single dopant on CQD properties. There is very limited prior work focused on comparing the physicochemical and optoelectronic properties of N-CQDs synthesized from different isomers of a single type of nitrogen doping agent.

In this study, a bottom-up approach was employed to synthesize CQDs by transforming individual carbon atoms. Specifically, citric acid (CA) was utilized as the carbon source and converted into CQDs *via* microwave irradiation. Phenylenediamine (PD) isomers were employed as nitrogen-doping agents, as they have been proven to be efficient heteroatom sources for the synthesis of N-CQDs.[19] The high-energy microwaves facilitated rapid heating and decomposition of the carbon precursor, promoting the formation of CQDs through mechanisms such as dehydration and carbonization over a much shorter time period (minutes) *versus* other conventional methods like hydrothermal synthesis (several hours).[20,21]

To date, systematic studies isolating the effect of dopant regiochemistry on the physicochemical and optoelectronic properties of CQDs remain scarce.[22,23] In this regard, to examine the influence of dopant configuration on the properties of N-CQDs, three isomers of phenylenediamine (*i.e.*, *ortho*-, *meta*-, and *para*-phenylenediamine (*o*-PD, *m*-PD, and *p*-PD)) were employed as nitrogen doping agents, with citric acid serving as the carbon source. This approach enables a systematic investigation of how the relative position of amine groups within the dopant molecule governs nitrogen incorporation and, consequently, the physicochemical and optoelectronic properties of the synthesized N-CQDs.

Finally, to bridge the gap between fundamental nanomaterial design and practical application, it is essential to investigate the behavior of CQDs within polymer matrices. While the optical properties of CQDs are predominantly studied in solution, their performance can change significantly in the solid state due to aggregation, interfacial interactions, and restricted chain mobility.[24] Poly(vinyl alcohol) (PVA) was selected as the model polymer matrix in this work because of its excellent film-forming ability, optical transparency,

hydrophilicity, and strong intermolecular hydrogen bonding capability.[25,26] The abundant hydroxyl groups in PVA enable favorable interactions with the surface functional groups of CQDs, which can enhance dispersion, suppress aggregation, and stabilize their optoelectronic properties in the solid state. Studying the incorporation of N-CQDs into a PVA matrix therefore provides critical insight into how dopant configuration influences not only the intrinsic optical behavior of CQDs, but also their dispersion, UV-shielding efficiency, and functional performance in polymer nanocomposites. Such understanding is crucial for the rational design of CQD-based polymer films for advanced applications, including transparent UV-protective coatings and optoelectronic materials.

2 Experimental

2 1 Materials and reagents

Citric acid (ACS grade, MW 192.13 g mol^{-1}, CAS 77-92-9) was obtained from VWR chemicals, LLC (Radnor, PA, USA). *o*-Phenylenediamine (*o*-PD, 98%, CAS No. 95-54-5), *m*-Phenylenediamine (*m*-PD, 98%, CAS No. 108-45-2), and *p*-phenylenediamine (*p*-PD, 97%, CAS 106-50-3) were purchased from Thermo Scientific (Waltham, MA, USA). All phenylenediamine isomers ($C_6H_8N_2$, M_r = 108.14) were supplied in flake form. Poly(vinyl alcohol) (PVA, 99+% hydrolyzed, average $M_w \approx 50\,000$ g mol^{-1}, CAS 9002-89-5) was purchased from Aldrich Chemical company, Inc. (Milwaukee, WI, USA). All chemicals were used as received without further purification. Distilled water was utilized to ensure purity in the reactions.

2.2 Synthesis of nitrogen-doped CQDs (N-CQDs)

N-CQDs were prepared through a simple one-step microwave-assisted method. Initially, 1 g of citric acid (CA), serving as the carbon source, was dissolved in 50 mL of double-distilled water at 60 °C under continuous stirring for approximately 30 minutes. Next, *o*-/*m*-/or *p*-phenylenediamine (PD), used as the nitrogen-doping agent, was added to achieve an equimolar ratio between the carbon source and the nitrogen dopant in the precursor mixture. After cooling the solution to room temperature, the resulting solution was then subjected to microwave irradiation at 800 W for 10 minutes to complete the reaction. Subsequently, 20 mL of double-distilled water was added to the beaker containing the deposited N-CQD film. The mixture was sonicated in bath sonicator for 30 minutes and filtered through a 220 nm PTFE syringe filter. The resulting aqueous solution was dialyzed (dialysis bags 3.5 kDa, cellulose) for 48 hours to remove unreacted precursors and then freeze-dried for further characterization. The chemical structure and the preparation process of N-CQDs is schematically described in Fig. 1. The obtained samples were denoted as OP : CA, MP : CA, and PP : CA, indicating that equimolar amounts of *ortho*-, *meta*-, and *para*-phenylenediamine, respectively, and citric acid were used in the synthesis.

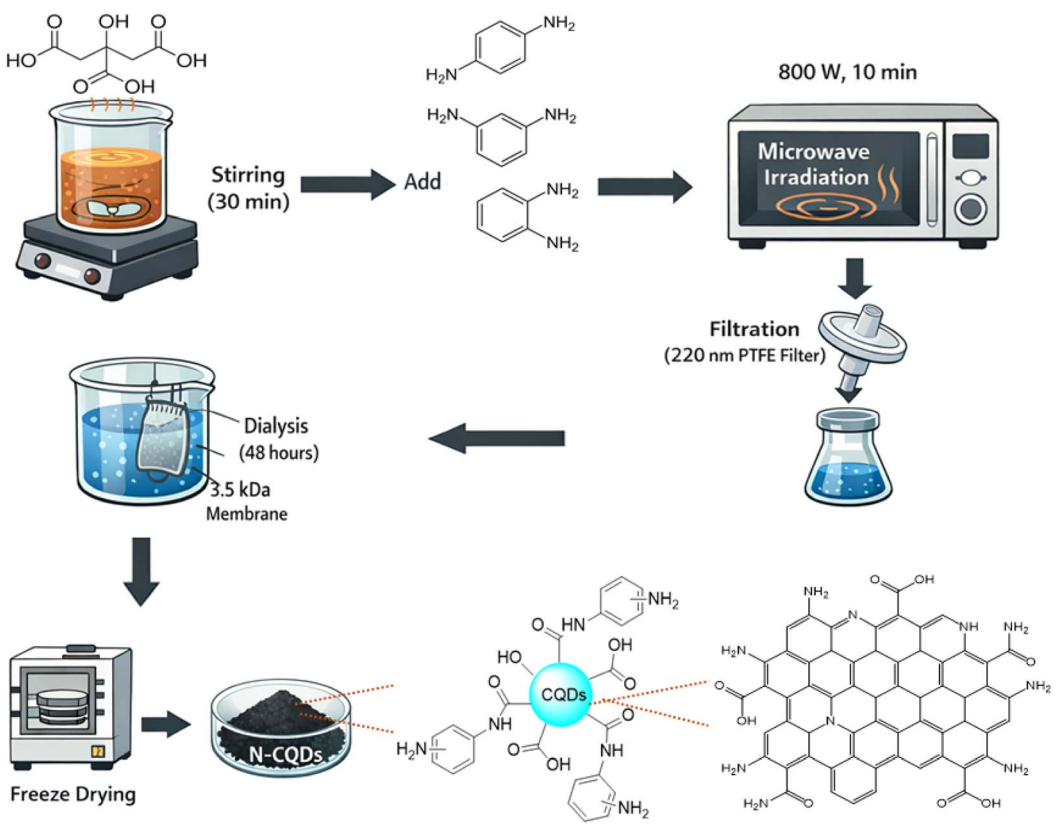

Fig. 1 Schematic representation of the microwave-assisted preparation of N-CQDs from citric acid and different isomers of phenylene diamine.

2.3 Fabrication of polyvinyl alcohol (PVA) nanocomposite films containing N-CQDs

The PVA/N-CQDs nanocomposite films were prepared by solution casting technique. 5 wt% N-CQDs and 95 wt% PVA were dissolved in distilled water and stirred at 75 °C for 30 minutes. The obtained solutions were sonicated for another 30 minutes using a bath sonicator and poured onto Petri dishes and dried at room temperature for 72 h. The solution concentration of PVA in water was 10 wt% and the final content of N-CQDs in PVA nanocomposite films was 5 wt%.

2.4 Characterization

Transmission electron microscopy (TEM) was conducted using Thermo Fisher Talos F200X G2 instrument with an accelerating voltage of up to 200 kV. to analyze morphology of the samples. X-ray photoelectron spectroscopy (XPS) (Thermo Scientific ESCALAB QXi) measurements were performed on a K Alpha plus X-ray photoelectron spectrometer equipped with an Al-Kα source to uncover the chemical compositions and distribution of surface functional groups. Fourier transform infrared (FTIR) spectroscopy was performed using the KBr pellet method on an Agilent Technologies FTIR spectrometer over the range of 400–4000 cm^{-1} to identify the surface functional groups of the synthesized samples. Ultraviolet-Visible (UV) absorption spectroscopy was performed with a UV-2600 (Shimadzu, Kyoto Japan) within wavelengths of 800 to 200 nm to characterize the optical properties of the synthesized CQDs. For this characterization, 0.07 mg ml^{-1} aqueous solutions of N-CQDs were prepared by dispersing CQDs powder in deionized water. In order to estimate the optical bandgap (E_g) of the synthesized CQDs, the following eqn (1) was applied based on the data obtained from UV-vis absorption spectra.

$$(\alpha h\nu)^{1/2} = A\,(h\nu - E_g) \quad (1)$$

where α is the absorption coefficient, h is the Planck constant, and ν is the frequency of the incident photon, and A is the slope of the linear region in the Tauc plot.[27]

The fluorescence spectra for 0.07 mg ml^{-1} CQDs solutions were measured on a Horiba FluoroMax-4 Spectrofluorimeter (New Jersey, United States) over the wavelength range from 300 to 600 nm at different excitation wavelengths, ranging from 280 to 400 nm with a 20 nm interval. An excitation and emission slit width of 3 nm was used.

To evaluate the fluorescence efficiency, the relative quantum yield of the samples (ϕ_s) was determined using eqn (2). This parameter was calculated by comparing the integrated fluorescence emission of the sample, excited at the same wavelength, with that of a reference standard possessing a known quantum yield (ϕ_r). For this purpose, quinine sulfate dissolved in 0.10 M H_2SO_4 aqueous solution was employed as the reference standard, with a reported quantum yield (ϕ_r) of 54%. In eqn (2), n_r and n_s denote the refractive indices of the reference solution and sample, respectively. The absorbance (A) refers to the optical density measured at 360 nm, while the photoluminescence intensity (PL) corresponds to the integrated area under the emission spectrum recorded over the wavelength range of 370–700 nm upon excitation at 360 nm.[28]

$$\varphi_s = \varphi_r \frac{A_r}{A_s} \frac{PL_s}{PL_r} \frac{{n_s}^2}{{n_r}^2} \quad (2)$$

Differential scanning calorimetry (DSC) is performed on a DSC Q500 (TA Instruments, New Castle, Delaware, USA) in nitrogen atmosphere to determine the crystallinity and melting temperature of the polymer nanocomposite films. The degree of crystallinity was calculated according to the following equation:

$$X_c = \frac{\Delta H_m}{\Delta H_m^0 \times W_f} \times 100 \quad (3)$$

where ΔH_m is the melting enthalpy obtained from DSC, W_f is the weight fraction of nanofiller in the composite, and ΔH_m^0 is the theoretical melting enthalpy for 100% crystalline PVA, taken as 138.6 J g^{-1}.[29]

Three tensile properties of the PVA nanocomposite films including ultimate tensile strength, tensile modulus and elongation at break are measured through tensile tests conducted according to "ASTM Standard Test Method for Tensile Properties of Thin Plastic Sheeting" D882[30] using an INSTRON 5965 universal testing machine (Norwood, MA, USA). The test specimens were prepared as rectangular strips with a width of 1 cm and a length of 4 cm. The tensile tests were performed at room temperature with a crosshead speed of 10 mm min^{-1}.

3 Results and discussion

3.1 The morphology and chemical properties of N-CQDs

High resolution TEM (HR-TEM) imaging revealed pronounced morphology differences among the synthesized N-CQDs. As shown in Fig. 2a and b equimolar citric acid and either *ortho*- or *meta*-phenylenediamine (*o*-PD or *m*-PD) under microwave-assisted synthesis, yield spherical particles with average diameters of approximately 7.63 ± 1.65 and 9.44 ± 2.31 nm respectively, as calculated from particle size distribution histograms. The OP:CA sample additionally exhibits lattice fringes with an interplanar spacing of ~0.22 nm, which can be attributed to graphitic carbon domains. In contrast, using *para*-isomer produces large carbon sheets (micrometer-scale lateral dimension), nearly 100 orders of magnitude larger than the N-CQDs obtained with *ortho*- and *meta*-isomers (OP : CA and MP : CA samples) as shown in Fig. 2c. Previous studies showed that by tuning the carbonization degree of citric acid by controlling heating duration, it is possible to selectively synthesize either graphene quantum dots or extended graphene-like sheets.[31] In other words, such carbon sheets can be obtained when synthesis conditions favor extended planar sp^2 growth. However, the mechanistic explanation for this in our work is more complex, as the synthesis involves phenylenediamine in addition to citric acid. We propose that the observed morphological differences can be rationalized by considering variations in condensation and nucleation pathways, which are influenced by the steric hindrance introduced by the regiochemistry of the dopant.

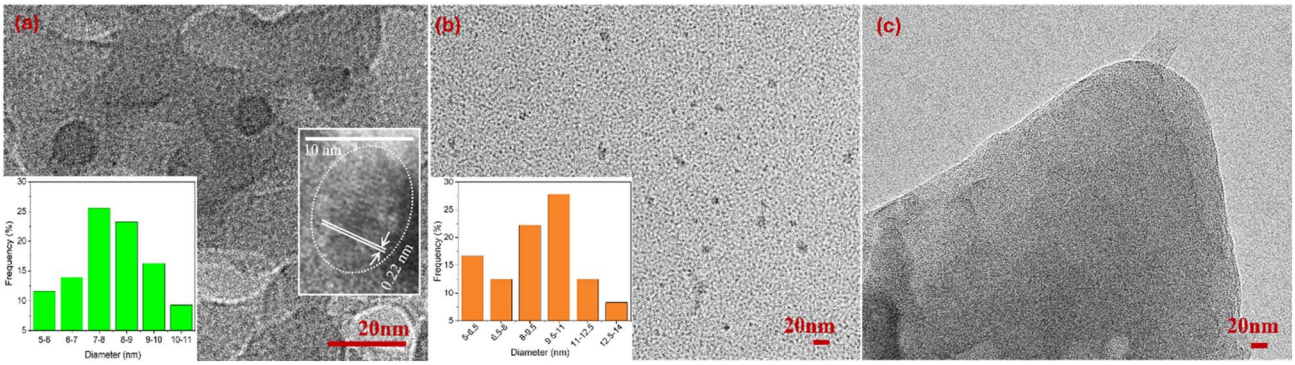

Fig. 2 HR-TEM images of nanoparticles synthesized using different phenylenediamine isomers as nitrogen-doping agent: (a) OP : CA, (b) MP : CA, and (c) PP : CA. Insets in (a) and (b) show the corresponding particle size distribution histograms for the N-CQDs. The inset in (a) also presents the lattice fringe of OP : CA.

In the microwave-assisted synthesis method (a bottom-up approach) the carboxylic acid groups of citric acid initially undergo condensation reactions with the amino groups of phenylenediamine isomers, to form polyamide intermediates. Subsequent crosslinking, dehydration, and irreversible carbonization of these nitrogen-containing polymeric carbonaceous intermediates lead to the nucleation of small sp^2-dominated carbon clusters. The formation of N-CQDs proceeds through surface functionalization processes, ultimately resulting in the termination and stabilization of nano sized carbon-based particles.[32] The pathway and efficiency of this nucleation step are dependent on the isomeric structure of the dopant.

The *o*- and *m*-PD isomers have two amine groups either on adjacent carbons (*o*-PD) or separated by one carbon (*m*-PD) on the phenyl ring. These geometries facilitate intramolecular condensation/oxidation pathways and form small, conjugated N-heterocyclic fluorophore species during the early reaction stages. These early nuclei then carbonize under microwave heating into small spherical N-doped CQDs. The restricted geometries of *o*- and *m*-PD also encourage more compact aggregation and hinder extended intermolecular alignment, further favoring isotropic particle growth.

In contrast, *p*-PD, with its two amine groups positioned at opposite ends of the aromatic ring, exhibits a molecular geometry that minimizes steric hindrance and makes early intramolecular cyclization significantly less favorable. Because the amine groups are spatially separated, *p*-PD is less likely to undergo localized ring closure and formation of compact N-heterocyclic fluorophore intermediates. Instead, this *para* configuration strongly favors intermolecular condensation and linear polymerization pathways, promoting the generation of extended polyaromatic intermediates with increasing conjugation length. Under the microwave-assisted conditions employed in this study, the combination of rapid volumetric heating, localized high-temperature regions, and relatively high *p*-PD precursor availability likely accelerates dehydration, aromatization, and coalescence of these intermediates before effective nanoscale nucleation and passivation can occur. Consequently, rather than terminating as discrete quantum-confined carbon dots, these extended intermediates undergo planar graphitization into micrometer-scale sp^2-rich carbon sheets. This mechanism distinguishes the present system from many previous hydrothermal syntheses, where slower reaction kinetics and different precursor stoichiometries more commonly favor controlled CQD nucleation.[22,23,33] Therefore, the unique sheet-like morphology observed for PP:CA is proposed to arise from the synergistic interplay of steric hindrance, enhanced intermolecular polymerization, high aromatic precursor concentration, and rapid microwave-induced carbonization. Recent studies on phenylenediamine-derived carbon nanomaterials further support the concept that isomer-dependent polymerization pathways strongly influence conjugation extent, graphitization behavior, and ultimate particle morphology, with *p*-PD generally promoting larger π-domains than *ortho*- or *meta*-isomers.[22,23,34]

Fig. 3 shows the FTIR spectrum of the synthesized particles, indicating the presence of characteristic nitrogen and oxygen

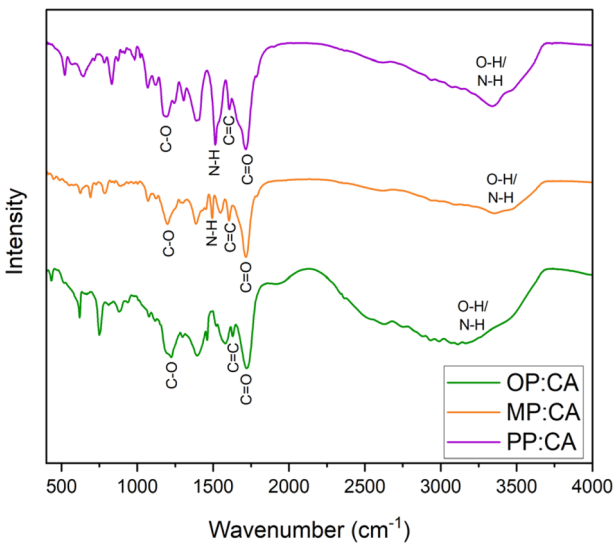

Fig. 3 FTIR spectra of nanoparticles doped with different isomers of phenylenediamine as the nitrogen doping agent.

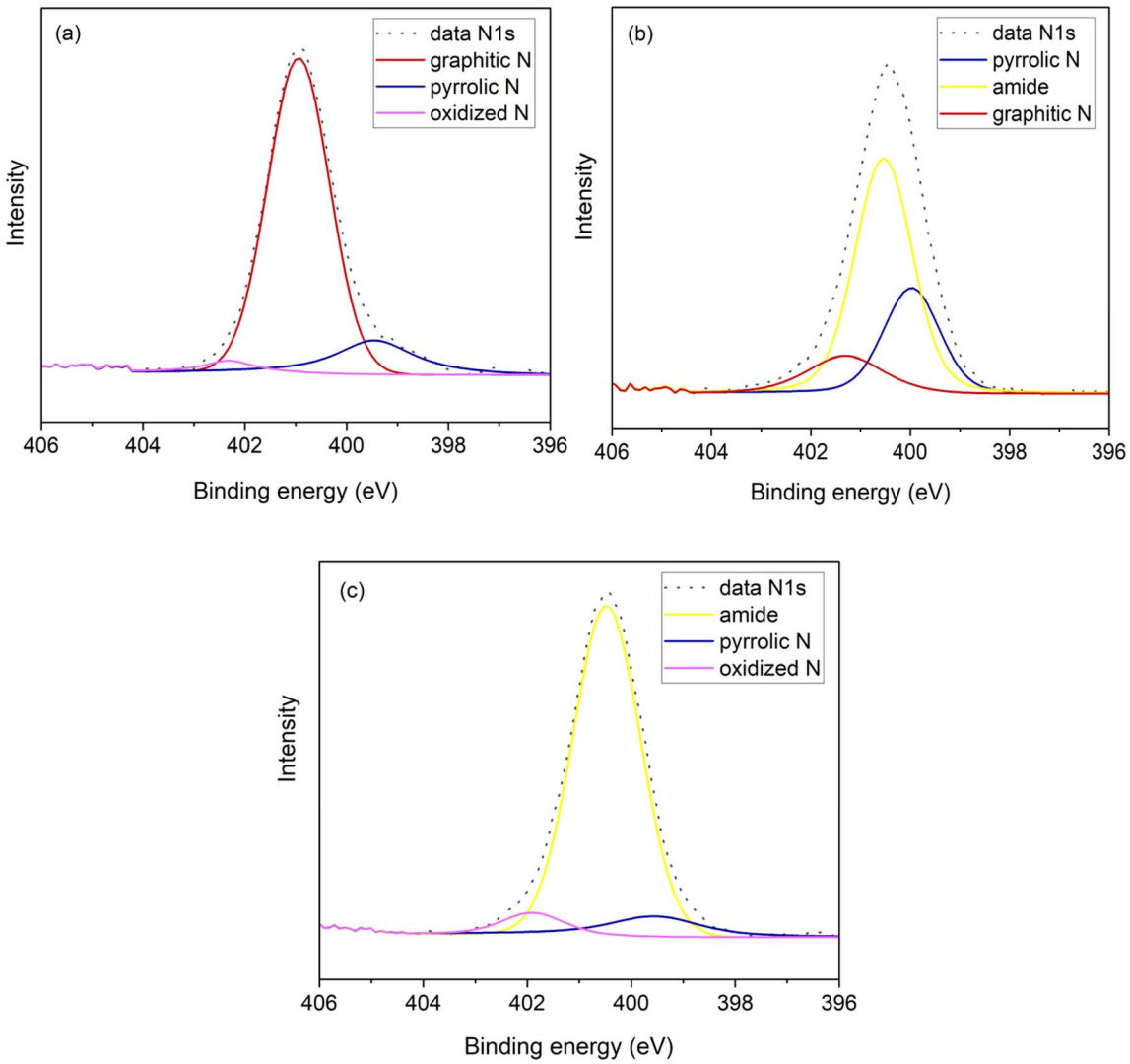

Fig. 4 The high resolution N 1s XPS spectra of nanoparticles doped with different isomers of phenylenediamine: (a) OP : CA, (b) MP : CA, and (c) PP : CA.

functional groups, which verifies successful nitrogen doping of the CQDs. A broad band observed in the 3100–3600 cm^{-1} region is attributed to overlapping O–H and N–H stretching vibrations, primarily arising from hydrogen-bonded hydroxyl groups, with possible contributions from nitrogen-containing functionalities.[35] These groups facilitate the dispersion of CQDs in aqueous media as well as in the PVA matrix through hydrogen bonding. The peak centered at around 1715 cm^{-1} is likely associated with the stretching vibration of carbonyl (C=O) functional groups.[15] The peaks in the range of 1625 to 1605 cm^{-1} are attributed to the C=C stretching vibrations or C–NH bending. Notably, PP:CA exhibits a pronounced absorption band at ~1513 cm^{-1}, while MP:CA shows a weaker band at ~1494 cm^{-1}. These bands can be assigned to N–H bending vibrations and/or amide II-type contributions, indicating the presence of surface amide/amine-related nitrogen functionalities. In contrast, OP : CA does not show a distinct band in the 1494–1513 cm^{-1} region; instead, it exhibits a weaker feature at ~1581 cm^{-1}, which is more reasonably attributed to aromatic C=C stretching within the conjugated sp^2 carbon network. This agrees with the predominance of graphitic nitrogen in OP:CA observed by XPS (see XPS results in Fig. 4) and suggests that nitrogen is mainly incorporated into the carbon framework rather than present as surface amide/amine groups. In the fingerprint region, the peaks at nearly 1390 and 1200 cm^{-1} confirm the presence of C–N and C–O bonds, respectively.[36]

The chemical structure can be determined using XPS analysis, and optical properties of N-CQDs have been shown to correlate closely with their chemical structure. Therefore, XPS was employed to better understand variations in the surface functional groups, the extent of nitrogen incorporation, and the position of nitrogen atom. The binding energy scale was calibrated using the C 1s standard value of 284.8 eV. The XPS survey spectra for all samples are shown in Fig. S1, which demonstrate three characteristic peaks around 285, 400 and 532 eV, corresponding to carbon (C 1s), nitrogen (N 1s) and oxygen (O 1s)

Table 1 Elemental composition and atomic ratios obtained from XPS analysis

Sample	C 1s (%)	O 1s (%)	N 1s (%)	O/C	N/C	Graphitic N (%)	Pyrrolic N (%)	Amide (%)	Oxidized N (%)
OP : CA	63.45	29.32	7.23	0.462	0.114	83	13.6	—	3.4
MP : CA	62.54	28.65	8.81	0.458	0.141	14.9	17.8	67.3	—
PP : CA	65.23	25.93	8.83	0.397	0.135	—	9.5	85	5.5

respectively.[17] The atomic percentage of carbon, nitrogen and oxygen resulting from the various configurations of the nitrogen doping agent is given in Table 1. The O/C atomic ratio shows the following sequence: OP : CA > MP : CA > PP : CA. This reveals that the location of $-NH_2$ groups within the three isomers impacts the oxidation level of the obtained nanoparticles. Accordingly, it can be concluded that PP : CA sample (doped with *p*-PD) contains less amount of oxygen functionalities, exhibiting lower hydrophilicity as compared to sample doped with *o*/*m*-PD. Meanwhile, the N/C ratios are relatively similar for all cases, indicating that using any of the three isomers results in comparable overall nitrogen levels.

The deconvolution of the high resolution N 1s spectra represented in Fig. 4a–c shows that the type of nitrogen incorporated into the carbon framework varies significantly with the isomer type. This spectra shows four components centered at approximately 399.5 eV, 400.5 eV, 401.2 eV, and 402.3 eV, tentatively attributed to pyrrolic N, amide, graphitic and oxidized N, respectively.[15,36] The N-CQD doped with *o*-PD exhibits predominantly graphitic nitrogen (83%), indicating that the nitrogen atoms are incorporated directly early on into the conjugated sp^2 lattice. The high fraction of graphitic N in OP : CA sample suggests that the *o*-PD isomer facilitates early intramolecular cyclization and formation of small aromatic *N*-heterocycles, which subsequently undergo carbonization into N-doped graphitic domains. This interpretation is also aligned with a study carried out by Dsouza *et al.*, which demonstrated that at lower carbonization rates, graphitic N dominates because nitrogen has sufficient time to enter the growing aromatic domains before extended polymerization occurs.[6]

As Fig. 4b shows, the sample doped with *m*-PD demonstrates a dramatic drop in graphitic N to 14.9%, with the majority (67%) of nitrogen present in the form of amide, which is usually located outside the core sp^2 lattice and a greater prevalence of nitrogen at defect sites or edges. This result is consistent with the slightly larger particle size observed in TEM and suggests that *m*-PD undergoes a mixture of intramolecular and intermolecular condensation processes, leading to less compact graphitic nuclei and more functionalized surfaces. According to Fig. 4c, the sample doped with *p*-PD shows no detectable graphitic nitrogen, with around 90% of nitrogen existing as surface bound species (85% amide and 5.5% oxidized N). This absence of graphitic N strongly supports the idea that *p*-PD does not form early N-containing aromatic nuclei but instead participates predominantly in intermolecular *para–para* polymerization, producing extended poly(*para*-phenylene)-like intermediates. During carbonization, such structures tend to planarize into large sp^2 sheets, but incorporate nitrogen only at defect sites and edges, rather than within the basal plane. This is consistent with the observed micrometer-scale sheet morphology and the lower O/C ratio for carbon nanosheets formed from *p*-PD. Similarly, Liu *et al.* showed that citric acid and the nitrogen doping agent compete to facilitate the growth of C and N atoms, and when the carbonization accelerates, the time window during which nitrogen can enter the core decreases. As a result, graphitic N decreases and surface-bound species increase.[15]

These findings strongly support the mechanistic interpretation that the regiochemistry of the phenylenediamine dopant governs early-stage condensation and nucleation pathways, thereby controlling nitrogen incorporation, degree of graphitization, and ultimately particle morphology.

3.2 The optical properties of N-CQDs

The optical absorption properties of the N-CQDs dispersed in colloidal solution were investigated using UV-vis spectroscopy. The corresponding spectra for samples prepared using the three PD isomers are presented in Fig. 5a–c. All samples exhibit a pronounced absorption band in the deep-UV region, with maximum wavelengths (λ_{max}) of 245, 235 and 253 nm for the *o*-, *m*- and *p*-PD-doped systems respectively. This high-energy band is attributed to $\pi \rightarrow \pi^*$transitions associated with aromatic sp^2-hybridized carbon domains formed during the carbonization of citric acid.[37,38] The presence of this feature in all samples indicates that their high-energy optical behavior is similar despite differences in final morphology (*i.e.*, CQDs *versus* sheet-like structure). This similarity exists because dehydration and carbonization of citric acid in the presence of PD isomers consistently produce aromatic sp^2 clusters, regardless of structural evolution during synthesis. As previously discussed, the aromatic nature of the phenylenediamine isomers facilitates the formation of extended conjugated networks, *i.e.*, the stable benzene ring in each precursor can be incorporated into the carbon framework without complete degradation.[17] Consequently, all three systems contain interconnected aromatic domains with alternating double bonds, enabling enhanced π-electron delocalization and thus strong UV absorption in the deep-UV region.

In contrast, notable differences are observed in the lower-energy region of the spectra. The samples doped with *o*- and *m*-PD exhibit a weak and broad absorption feature in the range of approximately 290–430 nm. This band can be attributed to $n \rightarrow \pi^*$ transitions associated with surface carbonyl (C=O) and nitrogen-containing (C–N) functional groups, which introduce localized electronic states within the carbon framework. Such

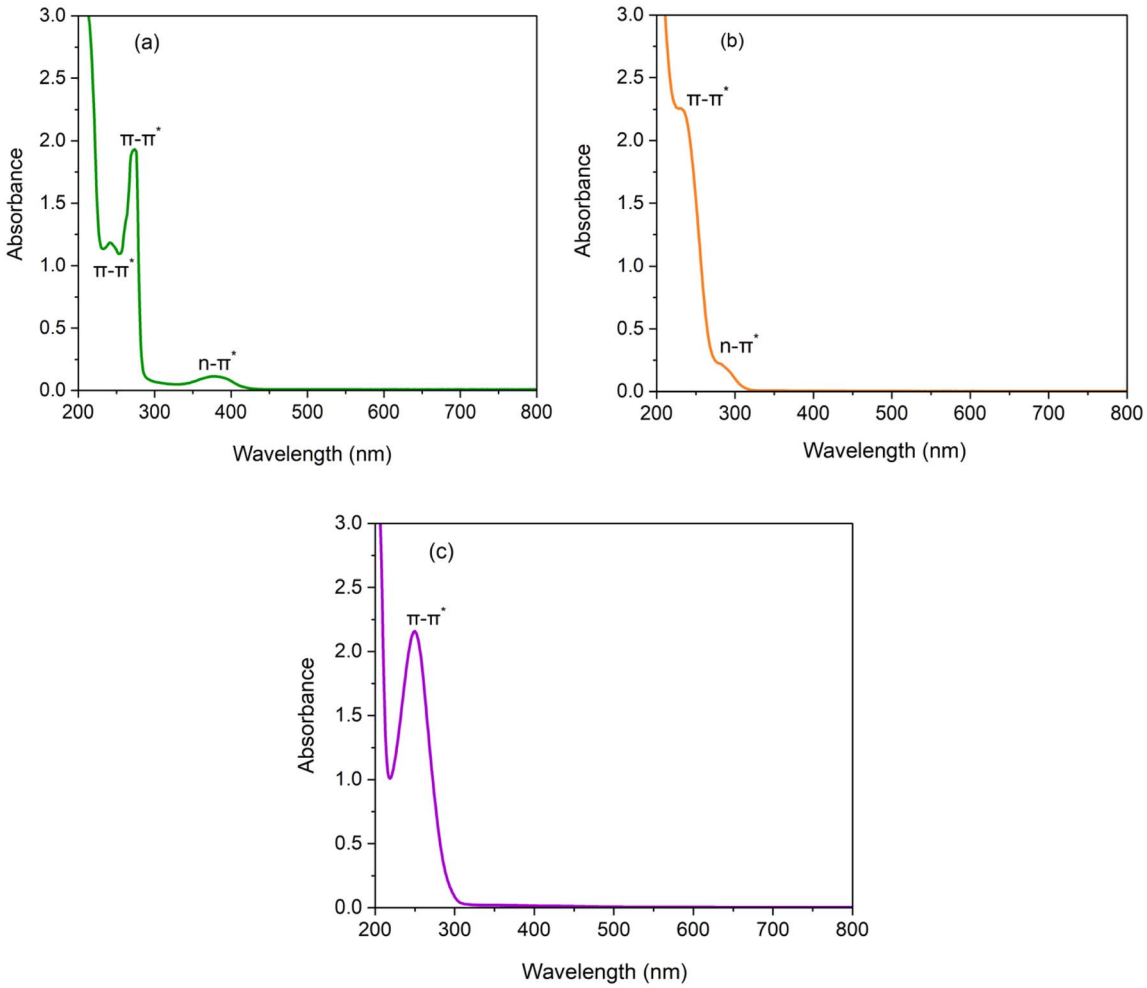

Fig. 5 UV-vis spectra of samples doped with different isomers of phenylenediamine: (a) OP : CA, (b) MP : CA, and (c) PP : CA.

transitions are commonly observed in heteroatom-doped carbon nanomaterials and are generally associated with surface defect states or functional groups.[39–41] As shown in Fig. 5c, the sample doped with *p*-PD, which consists predominantly of micrometer-scale aromatic sheets, does not display a distinct n → π* absorption feature. Tauc analysis (Fig. S2c) yields an apparent optical bandgap of 4.03 eV for this material, estimated under the assumption of an indirect allowed transition. The absence of a clear n → π* band in this sample is likely related to its higher degree of conjugation and graphitization, which reduces the density of localized surface states associated with heteroatom-containing functional groups. As electronic delocalization increases, discrete defect-related transitions become suppressed or indistinguishable within the broader π → π* absorption background.

The Tauc plots for the OP:CA and MP:CA samples (Fig. S2a and S2b), corresponding to N-CQDs doped with *o*- and *m*-PD, yield apparent optical bandgap values of 2.69 eV and 3.75 eV, respectively. Nitrogen incorporation is known to modify the electronic structure of carbon nanomaterials by introducing additional electronic states and altering the density of states near the band edges. The difference in bandgap values between the *o*- and *m*-PD-derived CQDs suggests that distinct nitrogen bonding configurations lead to different distributions of localized electronic states within the carbon framework.

The OP : CA sample exhibits an additional, more intense absorption peak centered at 275 nm, which can be assigned to an additional π → π*transition arising from larger or more highly conjugated aromatic domains. This is further enhanced by nitrogen incorporation from the precursor. XPS analysis indicates that this sample contains a significant fraction of graphitic nitrogen. Graphitic nitrogen is known to modify the electronic density of states near the conduction band and enhance π-electron delocalization within the carbon lattice. Such electronic modulation can facilitate additional π → π* transitions and contribute to bandgap narrowing.[15] Sarkar *et al.* reported that pyridinic, pyrrolic, and amino nitrogen species do not exert a significant influence on the optical properties of CQDs, whereas graphitic nitrogen markedly reduces the HOMO–LUMO gap, thereby lowering the energies of the corresponding optical transitions.[42] Overall, the UV-vis results demonstrate that both structural morphology and nitrogen configuration play crucial roles in shaping the optical band

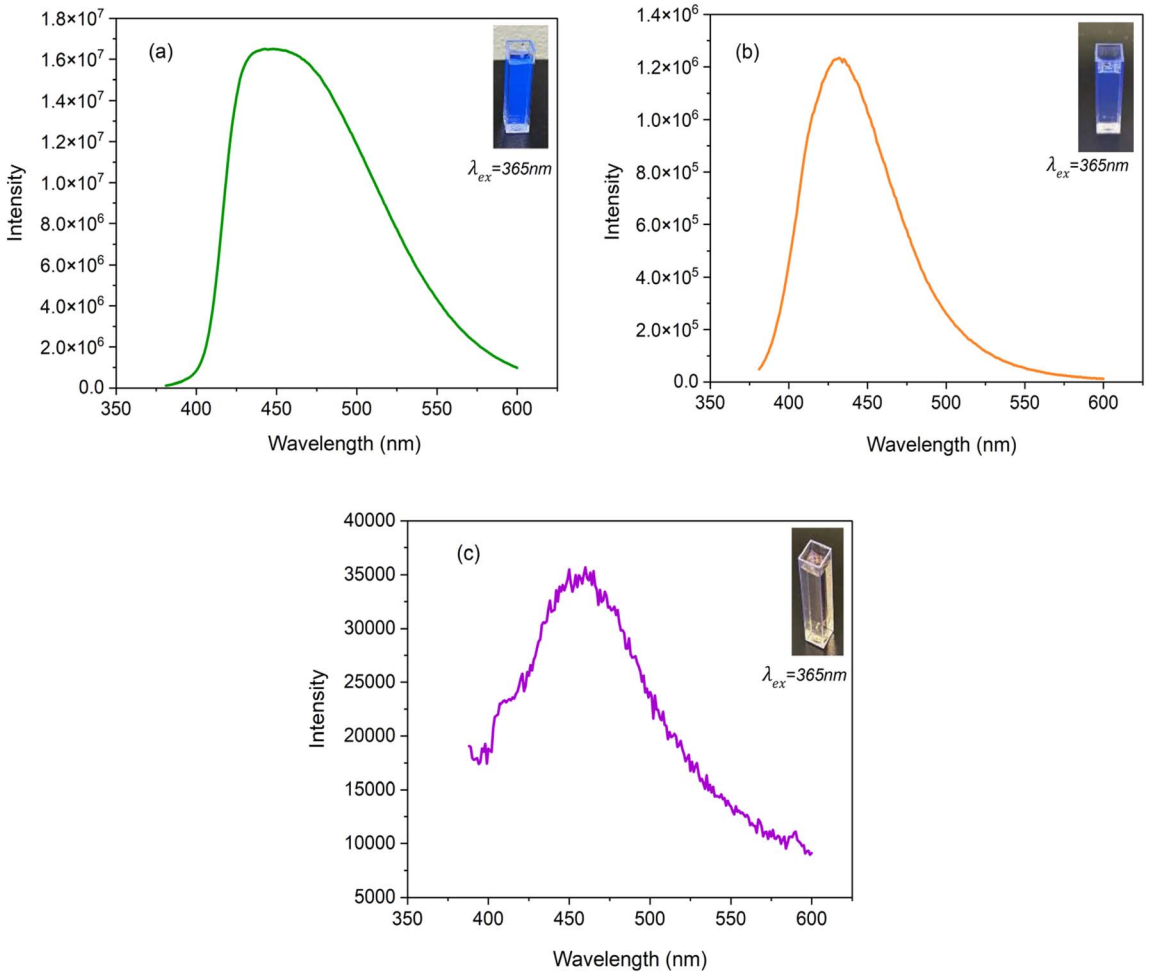

Fig. 6 Emission spectra of samples doped with different isomers of phenylenediamine: (a) OP : CA, (b) MP : CA, and (c) PP : CA.

structure and absorption characteristics of the synthesized nanomaterials.

Fig. 6a–c demonstrate the fluorescence spectra of three suspensions of nanoparticles in water obtained from *o*-/*m*- and *p*-PD as doping agent excited at 360 nm. It is important to note that the OP : CA sample emits the highest fluorescence intensity as compared to other samples. The insets of Fig. 6a and b which is the image of the suspension of N-CQDs excited *via* UV lamp show that both OP:CA and MP:CA samples are capable of emitting bright blue color which is more intense for the OP:CA sample.

In contrast, the *para*-isomer promotes formation of large carbon sheets rather than quantum-confined clusters. Since those large sheets lack the quantum-confined, discrete sp^2 islands that are responsible for fluorescence, the fluorescence is quenched and the product appears as non-emissive carbon sheets upon excitation using UV lamp as shown in Fig. 6c.

To further explore the influence of the dopant structure on the optical properties of the obtained N-CQDs, the QY values were evaluated according to eqn (2). Despite comparable nitrogen contents, the OP:CA sample exhibits a markedly higher QY (24%) than MP:CA (16%), while PP:CA sample shows a very low QY of 0.08%. This behavior can be attributed to differences in particle size, nitrogen bonding configuration, and electronic structure arising from the positional isomerism of the nitrogen precursor. As discussed earlier, the adjucent amine groups in *o*-PD can facilitate intramolecular cyclization and the formation of stable N-containing heterocyclic intermediates during the early stages of carbonization. This process favors the formation of compact graphitic domains with improved surface passivation, thereby promoting radiative electron–hole recombination and suppressing non-radiative decay pathways. This interpretation is consistent with the excitation-independent emission behavior observed for OP : CA (Fig. S3a), which suggests a relatively homogeneous electronic structure with fewer surface trap states. UV-vis spectroscopy further supports this interpretation. The OP:CA CQDs display two $\pi - \pi^*$ transitions together with an $n - \pi^*$ absorption transition centered at ~385 nm, which is shifted toward longer wavelength relative to the corresponding absorption feature of MP:CA, indicative of extended π-conjugation and a reduced optical bandgap. Graphitic nitrogen is known to modify the electronic density of states near the band edges, enhance π-electron delocalization, and contribute to bandgap narrowing, while also reducing

defect-mediated non-radiative recombination. Collectively, these effects contribute to the enhanced photoluminescence efficiency of OP:CA. In contrast, *m*-PD with spatially separated amine groups, is less prone to cyclization and tends to introduce non-radiative defect states, which act as quenching centers and reduce emission efficiency. Fig. S3b which represents excitation dependent behavior in the emission spectra of MP:CA sample supports this explanation.

To clarify the role of nitrogen doping, undoped CQDs were synthesized from citric acid under identical conditions. This sample exhibits a larger optical bandgap (~4.1 eV) and absorption mainly in the deep-UV region (Fig. S4 and S5), whereas N-doped CQDs showed bandgap narrowing and more pronounced n → π* transitions. Photoluminescence measurements (Fig. S6) reveals broad, excitation-dependent emission for undoped CQDs, in contrast to the enhanced and more excitation-independent emission observed for OP : CA, with MP : CA showing intermediate behavior. These results confirm that nitrogen incorporation, and its specific configuration, significantly modifies the electronic structure and photophysical properties of CQDs.

3.3 proposed molecular-level structural models

To further rationalize the observed structure–property relationships, schematic molecular-level structural models for the three synthesized nanomaterials are proposed. For the OP : CA sample, the structure is envisioned as a compact quasi-spherical CQD composed of small sp^2-hybridized graphitic domains, where nitrogen atoms are predominantly incorporated substitutionally as graphitic N within the basal plane. This architecture is likely facilitated by the adjacent amine groups of *o*-PD, which promote early intramolecular cyclization and the formation of small N-containing heterocyclic intermediates prior to carbonization. The resulting graphitic core is surrounded by a relatively thin shell of oxygen-containing functional groups such as hydroxyl and carboxyl groups. In contrast, the MP : CA sample is proposed to possess a less ordered sp^2 carbon core, in which nitrogen is primarily present as amide and pyrrolic species localized at edge sites and structural defects. Because the *meta* configuration is less favorable for efficient intramolecular cyclization, carbonization proceeds through more surface-dominated condensation pathways, resulting in a greater density of functional groups and defect states. These structural features contribute to stronger surface-state-mediated optical behavior.

For the PP : CA sample, the *para* configuration promotes more linear intermolecular polymerization and extended conjugation, favoring the formation of planar aromatic polymeric intermediates that subsequently carbonize into micrometer-scale carbon nanosheets rather than discrete CQDs. Accordingly, this structure is better described as extended planar sp^2 carbon sheets, where nitrogen is incorporated predominantly at edge or defect sites in the form of amide and oxidized species. Fig. S7 shows a schematic representation of the core chemical structures and dominant nitrogen configurations of the three synthesized materials, illustrating how dopant regiochemistry governs final nanomaterial architecture. It is worth mentioning that these proposed structures are mechanistic models derived from combined spectroscopic and morphological evidence rather than definitive molecular structures.

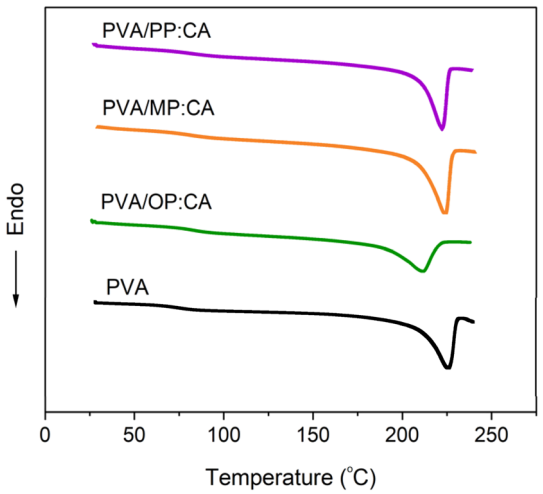

Fig. 7 DSC curves for neat PVA and PVA nanocomposite samples containing 5 wt% nanofillers derived from different PD isomers.

3.4 Thermal and mechanical properties of PVA nanocomposite films

The DSC thermograms of the PVA-based nanocomposite films, as shown in Fig. 7, demonstrate how the morphology of the obtained nanoparticles, dictated by the PD isomer, affects the polymer's thermal behavior and crystallization and Table 2 reports the DSC data. Table 2 shows that pure PVA displays a melting temperature (T_m) of 226.2 °C, a melting enthalpy of 36.9 J g^{-1}, and a crystallinity of 26.7%, typical of semi-crystalline PVA.

Adding OP : CA CQDs causes a strong T_m depression to 212.4 °C, while the melting enthalpy and crystallinity remain close to those of pure PVA. This suggests that although the small spherical *o*-PD-derived CQDs interact sufficiently with PVA chains to disrupt crystal perfection, which leads to the lower melting point, they do not significantly alter the number of crystallizable domains. The nearly unchanged crystallinity implies that these fillers behave mainly as defect sites within existing lamellae rather than strong nucleating agents.

In contrast, the slightly larger spherical MP : CA CQDs keep T_m close to that of pure PVA but significantly raise the melting

Table 2 Parameters obtained by DSC of PVA and its nanocomposites

	T_m (°C)	ΔH_m (J g^{-1})	X_C (%)
PVA	226.2	36.9	26.7
PVA/OP : CA	212.4	36.4	27.8
PVA/MP : CA	223.9	51.6	39.3
PVA/PP : CA	222.7	47.9	36.5

enthalpy to 51.6 J g^{-1} and crystallinity to 39.3%. These CQDs function as effective nucleation centers, promoting the formation of more crystalline domains without significantly altering lamellar stability. The larger particle size and potentially better distribution may facilitate stronger interfacial interactions with PVA, enabling more orderly chain packing during solidification. The *p*-PD – derived carbon sheets (PP : CA sample) produces a similar, though slightly weaker, nucleating effect. T_m decreases only slightly (222.7 °C), while the melting enthalpy increases to 47.9 J g^{-1}, giving a crystallinity of 36.5%. Their large 2D surfaces likely enhance chain alignment despite some chain restriction which led to crystal imperfection.

It is worth mentioning that the degree of crystallinity can influence how a polymer interacts with UV radiation. Although UV blocking is primarily governed by the optical properties of the fillers, the polymer matrix and particularly its crystallinity can affect light propagation within the material. Crystalline regions possess a more ordered molecular structure and a refractive index distinct from that of the surrounding amorphous phase. The resulting refractive-index contrast can enhance light scattering, leading to reduced UV transmittance.[5] Crystallinity also can affect the long-term durability of polymer films. More crystalline materials have reduced chain mobility and fewer amorphous regions, which are generally more susceptible to photo-oxidative degradation.[43] Consequently, high crystallinity tends to slow UV-induced chain scission, oxidation, and overall aging which is favorable for UV-blocking films.

The effects of N-CQDs and carbon nanosheets on the mechanical properties of PVA films were investigated by tensile testing, and the results are shown in Fig. 8 and Table 3. Incorporation of OP : CA CQDs modestly increases the elastic modulus (2286 MPa) and tensile strength (50.3 MPa) compared to pure PVA (1965 MPa, 37.6 MPa respectively) while also substantially enhancing elongation at break (26.3% *vs.* 19.6%). This suggests that the OP:CA CQDs act as effective stress-transfer points and provide flexibility, likely due to their uniform dispersion and minimal restriction of polymer chain mobility, consistent with the near-unchanged crystallinity observed from DSC. For MP:CA CQDs, the elastic modulus (3542 MPa) and tensile strength (57.4 MPa) increases significantly, whereas elongation at break drops sharply to 5.8%. This behavior can be attributed to the higher degree of crystallinity (39.3%) revealed by DSC, which enhances stiffness and load-bearing capacity but restricts chain mobility, reducing ductility.

Table 3 Mechanical properties of neat PVA and PVA nanocomposite samples containing 5 wt%. Nanofillers derived from different isomers of PD

	Elastic modulus (MPa)	Tensile strength (MPa)	Strain at break (%)
PVA	1965 ± 58	37.6 ± 1.8	19.6 ± 1.7
PVA/OP : CA	2286 ± 77	50.3 ± 3.7	26.3 ± 2.2
PVA/MP : CA	3542 ± 189	57.4 ± 4.1	5.8 ± 1.8
PVA/PP : CA	3410 ± 107	34.7 ± 3.9	4.3 ± 0.6

On the other hand, PP : CA carbon sheets produce a similar increase in modulus (3410 MPa) but a lower tensile strength (34.7 MPa) and a very low elongation at break (4.3%). The large, planar morphology (micrometer-scale sheets) likely disrupts stress transfer efficiency and introduces stress concentration points, despite the relatively high crystallinity (36.5%). Here, the 2D sheets contribute to stiffness through physical hindrance but compromise the tensile strength and toughness/flexibility of the films.

3.5 UV-vis transmittance performance of PVA nanocomposite films

Fig. 9 displays the influence of filler type on the UV-vis transmittance of PVA nanocomposite films. The incorporation of nanofillers significantly reduces the UV transmittance of neat PVA in the UV-C region (200–280 nm), which is attributed to conjugated aromatic structures that absorb high-energy radiation. Despite this reduction in UV transmission, all nanocomposite films retain high transparency in the visible region, likely due to uniform filler dispersion facilitated by hydrogen-bonding interactions between PVA chains and hydrophilic surface groups. Although many polymer films with high UV-shielding efficiency have been reported, they often suffer from reduced visible-light transparency, limiting practical

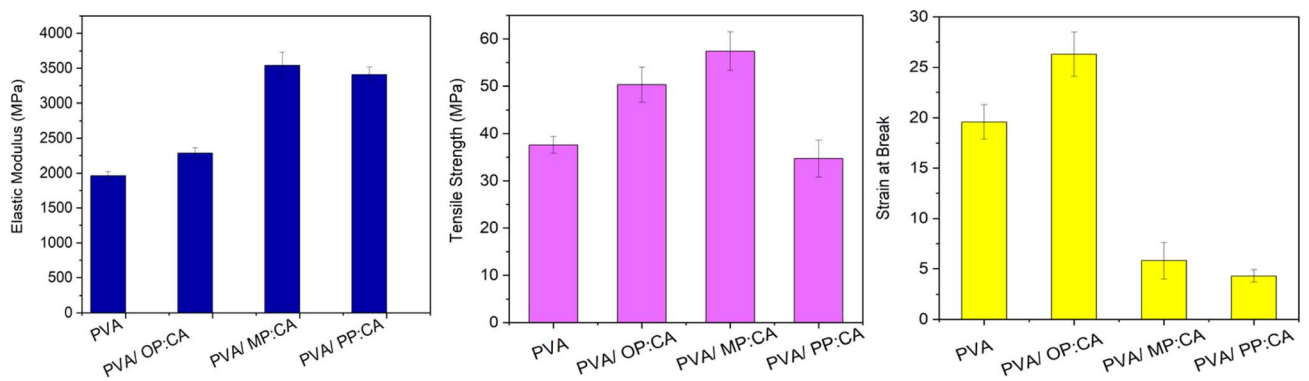

Fig. 8 Mechanical properties of neat PVA and PVA nanocomposite samples containing 5 wt% nanofillers derived from different isomers of PD.

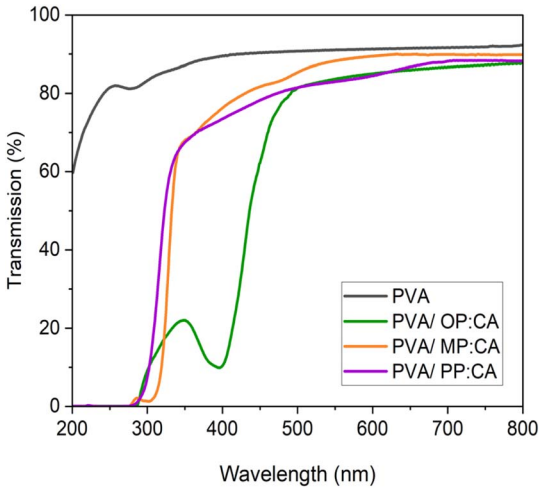

Fig. 9 Transmittancs graphs for neat PVA and PVA nanocomposite samples containing 5 wt% nanofillers derived from different isomers of PD.

applications.[44–47] In contrast, the films incorporating OP : CA and MP : CA CQDs exhibit high transparency in the visible spectrum while maintaining satisfactory UV-blocking performance.

The UV-shielding behavior of the polymer nanocomposite films can be described as follows. Upon UV exposure, a fraction of the incident light is reflected at the film surface, while the remainder penetrates the material and undergoes multiple scattering events at filler – matrix interfaces. Simultaneously, part of the radiation is absorbed by the nanofillers, with the residual fraction transmitted through the film.[5,48] As illustrated in Fig. 10, in CQD-containing nanocomposites, UV attenuation is dominated by light absorption arising from bandgap transitions between the valence and conduction bands.[49] In the present PVA-based system, UV-shielding is primarily governed by intrinsic electronic absorption, which depends on the nitrogen bonding configuration and resulting nanostructure

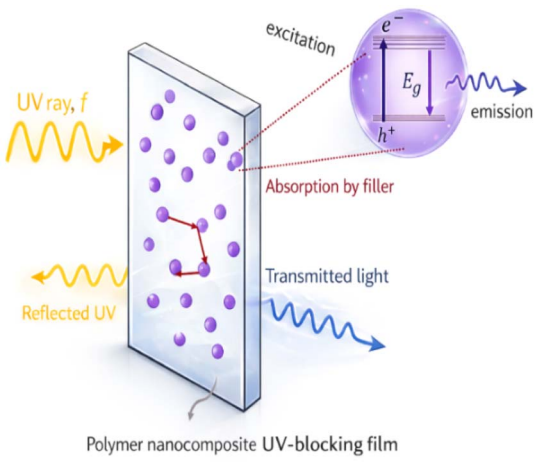

Fig. 10 Mechanism of UV shielding in polymer nanocomposites containing CQDs as filler.

that modulate the electronic structure and optical transitions of the nanofillers.

The nanocomposite film containing OP : CA, exhibits effective UV-shielding performance, blocking around 90% of long-wavelength UV radiation at 400 nm. This enhanced UV attenuation is primarily attributed to bandgap narrowing induced by the incorporation of graphitic nitrogen. XPS analysis revealed a high fraction of graphitic nitrogen (83%), which promotes π-electron delocalization and thereby modifying the electronic density of states near the band edges. As a result, the optical bandgap is reduced, enabling efficient absorption of longer-wavelength UV photons.[6,50] In addition, the observed red-shifted $n \rightarrow \pi^*$ transition in the UV-vis spectra is associated with defect/surface states introducing localized electronic states that further broaden the absorption range. However, these surface-state contributions are secondary to band structure modification. This is supported by the excitation-independent emission of OP : CA (Fig. S3), indicating a relatively homogeneous electronic structure with fewer surface trap states, consistent with bandgap narrowing as the dominant mechanism.

The PVA/MP : CA film demonstrates its maximum UV-blocking efficiency in the shorter wavelengths of UV-B region, with a peak at approximately 305 nm. The nitrogen doped into MP : CA CQDs is predominantly present in the form of amide N, which introduce localized electronic states within the bandgap. Since the optical bandgap of MP : CA CQDs is higher (3.75 eV) and dominant excitation-dependent behavior was observed for this filler (Fig. S3) reflecting a broader distribution of localized defect/surface states, the UV-blocking behavior is mainly governed by defect/surface-state absorption. Although OP : CA and MP : CA fillers both exhibit $n \rightarrow \pi^*$ absorption, their contributions to UV shielding occur in different spectral regions due to differences in electronic structure. In PVA/MP : CA, the predominance of amide-like and surface-bound nitrogen species introduces localized defect/surface states that contribute more strongly to absorption in the shorter-wavelength UV region, around 300 nm. In contrast, the higher graphitic nitrogen content and lower optical bandgap of OP : CA extend absorption toward longer wavelengths, leading to superior shielding near 400 nm. Moreover, UV-shielding is significantly stronger for the PVA/MP : CA nanocomposite at 300 nm than for the PVA/OP : CA system at 400 nm. It is worth noting that although increased crystallinity in semi-crystalline polymers can enhance light scattering due to refractive index mismatch between crystalline and amorphous domains, this effect is strongly wavelength-dependent and becomes more significant at longer wavelengths. In the UV region, particularly around 300 nm, absorption processes dominate due to the high photon energy, and therefore the contribution of scattering to UV attenuation is limited. Consequently, the enhanced UV-blocking observed in PVA/MP : CA at shorter wavelengths compared to PVA/OP : CA is primarily attributed to defect/surface-state absorption rather than crystallinity-induced scattering.

The nanocomposite film containing PP : CA nanoparticles, which lack dopant-induced interband states within the

bandgap (confirmed by UV-vis), does not exhibit pronounced UV-shielding efficiency at longer UV wavelengths. Nevertheless, its UV transmittance remains lower than that of neat PVA. For this sample, the UV-blocking behavior is dominated by $\pi \rightarrow \pi^*$ transitions within extended conjugated sp^2 domains. The higher degree of graphitization suppresses distinct localized n $\rightarrow \pi^*$ transitions, and the estimated optical bandgap (~4.03 eV) suggests limited bandgap narrowing. In this case, UV attenuation arises mainly from intrinsic absorption of high-energy UV photons by the conjugated carbon network, with a minor contribution from light scattering due to the larger size of the PP:CA particles.

Although internal scattering at filler – matrix interfaces may contribute to UV attenuation, it is not considered the dominant mechanism in these samples. This is supported by the high transparency of the nanocomposite films in the visible region, which indicates limited scattering losses.

4 Conclusions

In this work, we systematically demonstrated that the regiochemistry of a single nitrogen dopant precursor plays a decisive role in governing the nucleation pathway, nitrogen incorporation mechanism, and structure–property relationships of nitrogen-doped carbon quantum dots (N-CQDs). By employing *ortho*-, *meta*-, and *para*-phenylenediamine isomers in a microwave-assisted bottom-up synthesis, we isolated the effect of dopant configuration while maintaining comparable overall nitrogen contents. The results reveal that differences in amine positioning translate into profound variations in particle morphology, bonding configuration, and optoelectronic behavior.*o*- and *m*-PD favored the formation of discrete, spherical N-CQDs with the average size of 7.63 ± 1.65 and 9.44 ± 2.31 nm respectively, whereas the *p*-PD isomer promoted extended planar micrometer-scale carbon sheets, indicating fundamentally different condensation and carbonization pathways.

XPS analysis showed that *o*-PD predominantly yields graphitic nitrogen incorporated into the sp^2 lattice, while *m*-PD and *p*-PD introduce nitrogen mainly as surface-bound amide species. These differences directly control the electronic structure of the resulting materials, leading to excitation-independent, high-efficiency blue photoluminescence (QY of 24%) for OP:CA that was derived from *o*-PD, reduced emission efficiency (QY of 16%) for MP:CA derived from *m*-PD, and near-complete fluorescence quenching for *p*-PD – derived carbon sheets (PP:CA sample). Thus, different dopant regiochemistry leads to different optical behavior.

Embedding the N-CQDs into PVA matrices further demonstrated how dopant-dependent morphology and surface chemistry govern solid-state performance. Small *o*-PD – derived N-CQDs (OP : CA) preserved polymer flexibility while providing efficient broadband UV shielding (around 90% blocking UV-radiation at 400 nm) with high visible transparency, whereas *m*-PD – derived N-CQDs (MP : CA) enhanced crystallinity, stiffness, and UV-B blocking efficiency. In contrast, *p*-PD – derived carbon sheets (PP : CA) increased stiffness but compromised ductility and exhibited weaker long-wavelength UV shielding due to the absence of dopant-induced interband states.

Overall, this study establishes dopant regiochemistry as a critical and previously underexplored design parameter for tuning CQD structure, nitrogen bonding states, and interfacial behavior in polymer nanocomposites. The insights presented here provide a fundamental framework for the rational design of CQD-based materials with tailored optical, mechanical, and UV-shielding properties, advancing their potential for transparent protective coatings and optoelectronic applications.

Author contributions

The manuscript was written through contributions of all authors. All authors have given approval to the final version of the manuscript.

Conflicts of interest

The authors declare no competing financial interests.

Data availability

The original contributions presented in this study are included in the article. Further inquiries can be directed to the corresponding author.

Supplementary information (SI): additional characterization data and supporting analyses, including XPS survey spectra, Tauc plots, photoluminescence emission spectra, UV-vis spectra of undoped CQDs, and proposed molecular-level structural models for the synthesized nitrogen-doped carbon nanomaterials. See DOI: https://doi.org/10.1039/d6ra02179d.

Acknowledgements

We thank the Center for Advanced Polymers and Nanotechnology (CAPNA), Department of Chemical and Petroleum Engineering, University of Calgary, Canada, for the technical support. During the preparation of this work the authors used ChatGPT to improve the readability and language of the manuscript. After using this tool/service, the authors reviewed and edited the content as needed and took full responsibility for the content of the published article. Funding from Natural Sciences and Engineering Research Council of Canada (NSERC) Discovery Grant 2020-04058 is highly appreciated.

References

1 Ru Wang, K.-Q. Lu, Zi-R. Tang and Yi-J. Xu, Recent progress in carbon quantum dots: synthesis, properties and applications in photocatalysis, *J. Mater. Chem. A*, 2017, **5**(8), 3717–3734, DOI: 10.1039/C6TA08660H.

2 Z. Feng, K. H. Adolfsson, Y. Xu, H. Fang, M. Hakkarainen and M. Wu, Carbon dot/polymer nanocomposites: From green synthesis to energy, environmental and biomedical applications, *Sustain. Mater. Technol.*, 2021, **29**, e00304, DOI: 10.1016/j.susmat.2021.e00304.

3 A. S. Rasal, S. Yadav, A. Yadav, A. A. Kashale, S. Thagare Manjunatha, A. Ali and J.-Y. Chang, Carbon quantum dots for energy applications: a review, *ACS Appl. Nano Mater.*, 2021, **4**(7), 6515–6541, DOI: 10.1021/acsanm.1c01372.

4 S. Dua, P. Kumar, B. Pani, A. Kaur, M. Khanna and G. Bhatt, Stability of carbon quantum dots: a critical review, *RSC Adv.*, 2023, **13**(20), 13845–13861, DOI: 10.1039/D2RA07180K.

5 T. S. Muzata, A. Gebrekrstos, J. Tersur Orasugh and S. S. Ray, An overview of recent advances in polymer composites with improved UV-shielding properties, *J. Appl. Polym. Sci.*, 2023, **140**(14), e53693, DOI: 10.1002/app.53693.

6 S. D. Dsouza, M. Buerkle, P. Brunet, C. Maddi, D. Babu Padmanaban, A. Morelli, A. F. Payam, P. Maguire, D. Mariotti and V. Svrcek, The importance of surface states in N-doped carbon quantum dots, *Carbon*, 2021, **183**, 1–11, DOI: 10.1016/j.carbon.2021.06.088.

7 S. Paulo, E. Palomares and E. Martinez-Ferrero, Graphene and carbon quantum dot-based materials in photovoltaic devices: from synthesis to applications, *Nanomaterials*, 2016, **6**(9), 157, DOI: 10.3390/nano6090157.

8 G. Bharathi, D. Nataraj, S. Premkumar, M. Sowmiya, K. Senthilkumar, T. Daniel Thangadurai, O. Yu Khyzhun, *et al.*, Graphene Quantum Dot Solid Sheets: Strong blue-light-emitting & photocurrent-producing band-gap-opened nanostructures, *Sci. Rep.*, 2017, **7**(1), 10850, DOI: 10.1038/s41598-017-10534-4.

9 K. F. Mak, L. Ju, F. Wang and T. F. Heinz, Optical spectroscopy of graphene: From the far infrared to the ultraviolet, *Solid State Commun.*, 2012, **152**(15), 1341–1349, DOI: 10.1016/j.ssc.2012.04.064.

10 A. Ghaffarkhah, E. Hosseini, M. Kamkar, A. Akbari Sehat, S. Dordanihaghighi, A. Allahbakhsh, C. van der Kuur and M. Arjmand, Synthesis, applications, and prospects of graphene quantum dots: a comprehensive review, *Small*, 2022, **18**(2), 2102683, DOI: 10.1002/smll.202102683.

11 D. Ozyurt, M. Al Kobaisi, R. K. Hocking and B. Fox, Properties, synthesis, and applications of carbon dots: A review, *Carbon Trends*, 2023, **12**, 100276, DOI: 10.1016/j.cartre.2023.100276.

12 M. J. Molaei, Carbon quantum dots and their biomedical and therapeutic applications: a review, *RSC Adv.*, 2019, **9**(12), 6460–6481, DOI: 10.1039/C8RA08088G.

13 F. Mirlou-Miavagh, A. Rezvani-Moghaddam, H. Roghani-Mamaqani and U. Sundararaj, Comparative study of synthesis of carbon quantum dots via different routes: evaluating doping agents for enhanced photoluminescence emission, *Prog. Org. Coat.*, 2024, **191**, 108445, DOI: 10.1016/j.porgcoat.2024.108445.

14 F. Yan, Z. Sun, H. Zhang, X. Sun, Y. Jiang and Z. Bai, The fluorescence mechanism of carbon dots, and methods for tuning their emission color: a review, *Microchim. Acta*, 2019, **186**(8), 583, DOI: 10.1007/s00604-019-3688-y.

15 X. Liu, J. Yu, Y. Tan, W. Zhang, L. Zhu, S. Ye and J. Feng, Engineering nitrogen-doped carbon quantum dots: Nitrogen content-controlled dual-phase emission behavior, *J. Colloid Interface Sci.*, 2025, **686**, 951–959, DOI: 10.1016/j.jcis.2025.02.024.

16 L. Wang, X. Liu, P. Qi, J. Sun, S. Jiang, H. Li, X. Gu and S. Zhang, Enhancing the thermostability, UV shielding and antimicrobial activity of transparent chitosan film by carbon quantum dots containing N/P, *Carbohydr. Polym.*, 2022, **278**, 118957, DOI: 10.1016/j.carbpol.2021.118957.

17 S. Rosales, K. Zapata, O. E. Medina, B. A. Rojano, E. A. Taborda, F. B. Cortés, A. F. Pérez-Cadenas, E. Bailón-García, F. Carrasco-Marín and C. A. Franco, Effect of the chemical nature of the nitrogen source on the physicochemical and optoelectronic properties of carbon quantum dots (CQDs), *Nanoscale Adv.*, 2025, **7**(17), 5193–5211, DOI: 10.1039/D5NA00554J.

18 K. G. Nguyen, M. Huš, I. Alexandru Baragau, J. Bowen, T. Heil, A. Nicolaev, L. Elena Abramiuc, A. Sapelkin, M. T. Sajjad and S. Kellici, Engineering nitrogen-doped carbon quantum dots: tailoring optical and chemical properties through selection of nitrogen precursors, *Small*, 2024, **20**(24), 2310587, DOI: 10.1002/smll.202310587.

19 L. Wang, W. M. Choi, J. S. Chung and S. H. Hur, Multicolor emitting N-doped carbon dots derived from ascorbic acid and phenylenediamine precursors, *Nanoscale Res. Lett.*, 2020, **15**(1), 222, DOI: 10.1186/s11671-020-03453-3.

20 H. B. A. Sousa, C. S. M. Martins and J. A. V. Prior, You don't learn that in school: an updated practical guide to carbon quantum dots, *Nanomaterials*, 2021, **11**(3), 611, DOI: 10.3390/nano11030611.

21 R. K. Singh, R. Kumar, D. P. Singh, R. Savu and S. A. Moshkalev, Progress in microwave-assisted synthesis of quantum dots (graphene/carbon/semiconducting) for bioapplications: a review, *Mater. Today Chem.*, 2019, **12**, 282–314, DOI: 10.1016/j.mtchem.2019.03.001.

22 B. Li, T. Song, F. Cheng, L. Ren, Z. Jia, L. Song and C. Pu, Synthesis of multi-peak emitting carbon dots using phenylenediamine isomers, *Mater. Lett.*, 2025, **379**, 137693, DOI: 10.1016/j.matlet.2024.137693.

23 K. Jiang, S. Sun, L. Zhang, Y. Lu, A. Wu, C. Cai and H. Lin, Red, green, and blue luminescence by carbon dots: full-color emission tuning and multicolor cellular imaging, *Angew. Chem.*, 2015, **127**(18), 5450–5453, DOI: 10.1002/ange.201501193.

24 D. Sengottuvelu, K. S. Abdul, S. Mishra, H. Ahmad, M. Abbaszadeh, N. I. Hammer and S. Kundu, Multicolor nitrogen-doped carbon quantum dots for environment-dependent emission tuning, *ACS Omega*, 2022, **7**(31), 27742–27754, DOI: 10.1021/acsomega.2c03912.

25 R. Gao, X. Yi, X. Liu, H. Wang, L. Wang, B. Zeng, G. Chen, Y. Xu, C. Yuan and L. Dai, Phosphorus-doped carbon dots as an effective flame retardant for transparent PVA composite films with enhanced UV shielding property, *React. Funct. Polym.*, 2024, **197**, 105877, DOI: 10.1016/j.reactfunctpolym.2024.105877.

26 A. A. Oun, G. H. Shin, J.-W. Rhim and T. K. Jun, Recent advances in polyvinyl alcohol-based composite films and their applications in food packaging, *Food Packag. Shelf Life*, 2022, **34**, 100991, DOI: 10.1016/j.fpsl.2022.100991.

27 F. Zeng, C. Ji, Z. Xiang, L. Gao, W. Xu and Z. Peng, Optical Band Gap Determination of Carbon Dots: A Critical

Comparison of Tangent and Tauc Plot Methods Benchmarked with Metal Oxides, *Carbon*, 2026, 121239, DOI: 10.1016/j.carbon.2026.121239.

28 V. B. Kumar, S. K. Mirsky, N. T. Shaked and E. Gazit, High quantum yield amino acid carbon quantum dots with unparalleled refractive index, *ACS Nano*, 2024, **18**(3), 2421–2433, DOI: 10.1021/acsnano.3c10792.

29 A. K. Patel, R. Bajpai and J. M. Keller, On the crystallinity of PVA/palm leaf biocomposite using DSC and XRD Techniques, *Microsyst. Technol.*, 2014, **20**(1), 41–49, DOI: 10.1007/s00542-013-1882-0.

30 B. H. Musa and N. J. Hameed, Study of the mechanical properties of polyvinyl alcohol/starch blends, *Mater. Today: Proc.*, 2020, **20**, 439–442, DOI: 10.1016/j.matpr.2019.09.161.

31 Y. Dong, J. Shao, C. Chen, H. Li, R. Wang, Y. Chi, X. Lin and G. Chen, Blue luminescent graphene quantum dots and graphene oxide prepared by tuning the carbonization degree of citric acid, *Carbon*, 2012, **50**(12), 4738–4743, DOI: 10.1016/j.carbon.2012.06.002.

32 V. Hinterberger, W. Wang, C. Damm, S. Wawra, M. Thoma and W. Peukert, Microwave-assisted one-step synthesis of white light-emitting carbon dot suspensions, *Opt. Mater.*, 2018, **80**, 110–119, DOI: 10.1016/j.optmat.2018.04.039.

33 Q. Wang, Z. Pu, Y. Wang and M. Li, Surface passivated p-phenylenediamine carbon quantum dots (p-CQDs) as fluorescent turn-on probes for the detection of Li+ and L-arginine by two different mechanisms, *Opt. Mater.*, 2023, **136**, 113415, DOI: 10.1016/j.optmat.2022.113415.

34 F. Yan, J. Li, X. Zhao and X. Gong, Unveiling unconventional luminescence behavior of multicolor carbon dots derived from phenylenediamine, *J. Phys. Chem. Lett.*, 2023, **14**(26), 5975–5984, DOI: 10.1021/acs.jpclett.3c01497.

35 S. Yan, S. Yang, L. He, C. Ye, X. Song and F. Liao, Quantum size effect of poly (o-phenylenediamine) quantum dots: From controllable fabrication to tunable photoluminescence properties, *Synth. Met.*, 2014, **198**, 142–149, DOI: 10.1016/j.synthmet.2014.10.014.

36 Po-C. Yang, Yu-X. Ting, S. Gu, Y. A. Gandomi and C.-Te Hsieh, Fluorescent nitrogen-doped carbon nanodots synthesized through a hydrothermal method with different isomers, *J. Taiwan Inst. Chem. Eng.*, 2021, **123**, 302–309, DOI: 10.1016/j.jtice.2021.05.017.

37 D. Dagar, B. P. Kafle, A. Ladan, V. Shanmuganathan, H. Teng and Y.-L. Lee, Selective recognition of ciprofloxacin by carbon quantum dots and their underlying mechanism, *Chem. Eng. J.*, 2026, 174227, DOI: 10.1016/j.cej.2026.174227.

38 B. Vercelli, R. Donnini, F. Ghezzi, A. Sansonetti, U. Giovanella and B. La Ferla, Nitrogen-doped carbon quantum dots obtained hydrothermally from citric acid and urea: The role of the specific nitrogen centers in their electrochemical and optical responses, *Electrochim. Acta*, 2021, **387**, 138557, DOI: 10.1016/j.electacta.2021.138557.

39 P. K. Yadav, S. Chandra, V. Kumar, D. Kumar and S. H. Hasan, Carbon quantum dots: synthesis, structure, properties, and catalytic applications for organic synthesis, *Catalysts*, 2023, **13**(2), 422, DOI: 10.3390/catal13020422.

40 M. Beigi, M. Saberi, A. Rezvani-Moghaddam and H. Roghani-Mamaqani, Fluorescent carbon quantum dots from walnut green husk waste: Synthesis, characterization, and application in sustainable inkjet printing, *Biomass Bioenergy*, 2026, **207**, 108744, DOI: 10.1016/j.biombioe.2025.108744.

41 R. Rachmina, M. Hasan, S. Suhartono and M. I. Sulaiman, Enhanced Fluorescence and Heavy Metal Ion Sensing Using Nitrogen-Doped Carbon Quantum Dots Synthesized from Banana Peel Waste, *Results Eng.*, 2026, 109321, DOI: 10.1016/j.rineng.2026.109321.

42 S. Sarkar, M. Sudolska, M. Dubecky, C. J. Reckmeier, A. L. Rogach, R. Zboril and M. Otyepka, Graphitic nitrogen doping in carbon dots causes red-shifted absorption, *J. Phys. Chem. C*, 2016, **120**(2), 1303–1308, DOI: 10.1021/acs.jpcc.5b10186.

43 R. Pantani and A. Sorrentino, Influence of crystallinity on the biodegradation rate of injection-moulded poly(lactic acid) samples in controlled composting conditions, *Polym. Degrad. Stab.*, 2013, **98**(5), 1089–1096, DOI: 10.1016/j.polymdegradstab.2013.01.005.

44 S. W. Park, So Hui Im, W. T. Hong, H. K. Yang and Y. Kyung Jung, Lignin-derived carbon quantum dot/PVA films for totally blocking UV and high-energy blue light, *Int. J. Biol. Macromol.*, 2024, **268**, 131919, DOI: 10.1016/j.ijbiomac.2024.131919.

45 H. Zhang, X. Cheng, C. Liu, Z. Liu, L. Liu, C. Feng, J. Ju and Xi Yao, Ultraviolet-blocking polymers and composites: recent advances and future perspectives, *J. Mater. Chem. A*, 2024, **12**(47), 32638–32664, DOI: 10.1039/D4TA06335J.

46 A. I. Quilez-Molina, M. Lara, A. Athanassiou and I. S. Bayer, UV-blocking, transparent, and antioxidant polycyanoacrylate films, *Polymers*, 2020, **12**(9), 2011, DOI: 10.3390/polym12092011.

47 K. M. Lim, K. Z. Chiew, S. Y. Pung and W. S. Chow, UV-protective properties of poly (lactic acid) nanocomposites containing chemical treated halloysite nanotube, *Mater. Today: Proc.*, 2019, **17**, 853–863, DOI: 10.1016/j.matpr.2019.06.372.

48 A. Ahmed, B. Adak, T. Bansala and S. Mukhopadhyay, Green solvent processed cellulose/graphene oxide nanocomposite films with superior mechanical, thermal, and ultraviolet shielding properties, *ACS Appl. Mater. Interfaces*, 2019, **12**(1), 1687–1697, DOI: 10.1021/acsami.9b19686.

49 J. George and M. Balachandran, Oxygen surface-functionalized carbon dots derived from waste cassava peel for UV shielding applications, *Biomass Bioenergy*, 2026, **211**, 109221, DOI: 10.1016/j.biombioe.2026.109221.

50 M. Liu, Z. Liu, Z. Wen, N. Yu, D. K. Macharia, M. Zhu and Z. Chen, N-Doped Carbon-Quantum-Dot-Integrated Colorimetric System for Visible Photoprinting and Oxygen Sensing, *Adv. Opt. Mater.*, 2024, **12**(13), 2302787, DOI: 10.1002/adom.202302787.